Thermodynamical Effects of Ocean Current Feedback in a Quasigeostrophic Coupled Model

QUENTIN JAMET[,a] ALEXANDRE BERGER,[b] BRUNO DEREMBLE,[b] AND THIERRY PENDUFF[b]

[a] *INRIA, ODYSSEY Group, Ifremer, Plouzané, France*
[b] *Université Grenoble Alpes, CNRS, IRD, Grenoble INP, IGE, Grenoble, France*

ABSTRACT: Air–sea fluxes are the main drivers of ocean circulation, yet their representation in ocean-only models remains challenging. While a zeroth-order formulation accounting only for the state of the atmosphere is well adopted by the community, surface ocean feedback has gained attention over the last decades. In this paper, we focus on thermodynamical indirect feedback of surface ocean currents, which completes the "*eddy killing*" effect induced by the mechanical feedback. In this study, we quantify both the mechanical and thermodynamical contributions in the context of idealized, coupled quasigeostrophic simulations through sensitivity experiments on wind stress formulation. As compared to *eddy killing* which impacts kinetic energy levels, the indirect thermodynamical feedback induces significant changes in potential energy levels. The thermodynamical feedback also enhances by +27% the potential-to-kinetic turbulent energy conversion induced by relative wind stress formulation, as well as significant changes in both forward and inverse cascades of potential energy (PE). That is, accounting for ocean surface currents in the computation of wind stress significantly changes transfers of PE from the mean to the turbulent flow. These changes are mostly controlled by a reduced upscale energy flux rather than a more vigorous downscale flux, a process in line with results obtained for kinetic energy fluxes associated with the *eddy killing* effect.

KEYWORDS: Ocean dynamics; Ekman pumping; Atmosphere-ocean interaction; Energy budget/balance

1. Introduction

The large-scale oceanic circulations are in constant interaction with "eddies," the macroturbulent structures that develop in response to large-scale flow instabilities (McCaffrey et al. 2015). It is now widely recognized that eddies feed back part of their energy upscale and ultimately contribute in shaping large-scale oceanic currents (Deremble et al. 2023). This has motivated intensive work in the development of efficient/robust parameterizations of eddy–mean flow interactions for climate models. Most of our knowledge on these interactions is based on studies investigating these questions in the context of ocean-only simulations (e.g., Waterman and Jayne 2011; Kang and Curchitser 2015). However, air–sea interactions have the potential to modulate both the mean flow and the eddy field (Renault et al. 2016), hence their interactions.

In this paper, we are interested in quantifying the effects of dynamical and thermodynamical ocean–atmosphere coupling on the energetics of the mean flow and eddy flow. Our first focus is to quantify the impact of relative wind *vs.* absolute wind formulation of the ocean surface stress, one of the well-known mesoscale air–sea interaction processes (see Seo et al. 2023, for a recent review). Dewar and Flierl (1987) and Pacanowski (1987) were among the first to show the significant contribution of momentum air–sea feedback for ocean energetics. In its *relative* version, the magnitude of wind stress is proportional to the square of the difference between atmospheric winds and ocean surface currents:

$$\boldsymbol{\tau}_{\mathrm{rel}} = \rho_a C_D |\mathbf{u}_a - \mathbf{u}_o|(\mathbf{u}_a - \mathbf{u}_o), \tag{1}$$

with ρ_a as the density of air at sea level, C_D as the drag coefficient, $\mathbf{u}_a$ as the atmospheric wind at the surface of the ocean, and $\mathbf{u}_o$ as the ocean surface currents. In the development of ocean models, the wind stress was often formulated in its absolute version, i.e.,

$$\boldsymbol{\tau}_{\mathrm{abs}} = \rho_a C_D |\mathbf{u}_a|\mathbf{u}_a, \tag{2}$$

which is a zeroth-order approximation of air–sea momentum coupling assuming much larger surface winds [$\mathcal{O}(10)\mathrm{m\,s}^{-1}$] as compared to ocean surface currents [$\mathcal{O}(0.1)\mathrm{m\,s}^{-1}$]. However, formulating the wind stress with Eq. (1) or (2) can have drastic consequences on the ocean circulation.

Indeed, in the Ekman layer, the convergence of the Ekman transport results in an Ekman pumping (vertical velocity from the Ekman layer toward the ocean interior) or Ekman suction (vertical velocity from the ocean interior toward the Ekman layer). This vertical velocity is often computed as

$$w_{\mathrm{ek}} = \mathbf{k} \cdot \frac{\nabla \times \boldsymbol{\tau}}{f_0}, \tag{3}$$

with $\boldsymbol{\tau}$ as the surface stress computed following either Eq. (2) or (1).

As noted in Gaube et al. (2015), when computed with relative wind, one can decompose this Ekman pumping into a large-scale component and a small-scale component. The large-scale component is mostly due to the large-scale winds and can be considered as a forcing which results in the formation of large-scale oceanic gyres. On the other hand, the small-scale component is correlated with the presence of oceanic eddies and acts in two ways:

Corresponding author: Quentin Jamet, quentin.jamet@inria.fr

- First, the small-scale Ekman pumping induces a drag at the surface of the ocean and thus extracts surface ocean kinetic energy. This can be shown analytically by calculating the change in wind work (i.e., the mechanical energy input from the atmosphere to the ocean) induced by ocean surface current feedback and highlighting its negative definite contribution (see appendix D). Scaling arguments and numerical investigations (Dawe and Thompson 2006; Duhaut and Straub 2006; Song et al. 2020; Jullien et al. 2020; among others) suggest a reduction in the order of 20%–40% on basin-averaged estimates, with important regional variations depending on eddy activity.

  Renault et al. (2016) identified two main impacts of this *eddy killing* effect for the energetics of the North Atlantic subtropical gyre. First, through a reduced wind work in the tropics, the energy injected by the atmosphere into the ocean is reduced by about 30%. Jamet et al. (2021) also showed that the mean kinetic energy (KE) of the Gulf Stream is then reduced in response to a nonlocal inertial recirculation toward the western boundary dynamics. The Gulf Stream is then more stable and less prone to eddy generation. A second local impact of relative wind stress is to extract surface kinetic energy of ocean eddies downstream of the Gulf Stream separation, with a 27% reduction in the depth-integrated eddy KE (EKE) (Renault et al. 2016).

- Another effect that has not received a lot of attention is the thermodynamical consequences of this Ekman pumping. Indeed, the vertical velocity transports heat either from the mixed layer to the ocean interior or from the ocean interior to the mixed layer. For a well-defined eddy, this transport will always remove heat anomalies, damping the eddy (Gaube et al. 2015), and thus its associated available potential energy (APE). When accounting for ocean surface currents in wind stress formulation, eddies are thus damped by both mechanical (eddy killing) and thermodynamical (Ekman pumping) effects.

The main objective of this paper is to quantify and interpret the thermodynamical feedback for the ocean energy cycle in the context of idealized, coupled quasigeostrophic simulations. The paper is organized in the following way. In section 2, we first introduce the quasigeostrophic coupled model (Q-GCM) of Hogg et al. (2006) that we use for two simulations: one run with an absolute wind stress formulation following Eq. (2) and another run with a relative wind stress formulation following Eq. (1). In section 3, we quantify and discuss the wind stress contribution in these two simulations for both the kinetic and potential energy of the eddy field. As will be shown, the main effect of using a relative wind stress formulation is to change the turbulent wind work and turbulent diabatic heating forcing from sources to sinks of (kinetic and potential, respectively) energy, on average. Although the mechanical contribution of relative wind stress for EKE is not new, its thermodynamical contribution for eddy PE (EPE) has not received a lot of attention. In section 4, we analyze the consequence of the thermodynamical feedback for the energy transfers between different energy reservoirs, namely, the mean KE, eddy KE,

mean PE, and eddy PE, using the Lorenz energy cycle (LEC; Lorenz 1955; Harrison and Robinson 1978; Oort et al. 1994; Matsuta and Masumoto 2023) framework. We will pay a particular attention to the eddy potential-to-kinetic energy conversion as well as to the eddy–mean flow potential energy transfers. Still, in section 4, we also quantify and discuss the nonlocality associated with eddy–mean flow interactions, a characteristic that has been recently highlighted in several studies (e.g., Murakami 2011; Chen et al. 2014; Kang and Curchitser 2015; Matsuta and Masumoto 2021; Jamet et al. 2022), which is critical in order to interpret the spatial organization of eddy–mean flow energy transfers. We end this paper with a summary of main results and conclude on the extension of these results in the context of realistic modeling in section 5.

2. Methods

The Q-GCM

In this study, we investigate the exchanges of energy between the (temporal) mean and turbulent flow in an idealized, numerical framework. We use the Q-GCM (Hogg et al. 2006). This idealized coupled ocean–atmosphere model is meant to represent the dynamics of extratropical climate. It solves the quasigeostrophic potential vorticity (QGPV) equation in both the ocean and the atmosphere, and boundary layers are used to couple the system. The coupling involves Ekman dynamics, entrainment, and thermal exchanges. An additional Ekman layer is included in the bottom layer of the ocean, and lateral limits are treated as solid boundaries with mixed no-slip/free-slip conditions, expressed on pressure gradients (see Hogg et al. 2006, for details).

The setup is very similar to Martin et al. (2020). The (zonally periodic) atmosphere is horizontally discretized on 384×96 grid cells (64-km resolution) and the ocean on 1024×1024 grid cells (5-km resolution) for a square ocean basin dimension of 5120 km × 5120 km. Both fluids are vertically discretized with three layers, and the total depth of the ocean is 4 and 10 km for the atmosphere. The upper (bottom) ocean Ekman layer thickness is set to 100 m (5 m).

Following Hogg et al. (2014) and Martin et al. (2020), the quasigeostrophic vorticity equation solved by Q-GCM can be expressed in the following compact, vector form (we only recall the equations for the ocean):

$$\partial_t \mathbf{q} = \frac{1}{f_0} J(\mathbf{q}, \, \mathbf{p}) + \underline{\underline{\mathbf{B}}} \mathbf{e} - \frac{\mathcal{A}_4}{f_0} \nabla_H^6 \mathbf{p}, \qquad (4)$$

with

$$\mathbf{q} = \beta(y - y_0) + \frac{1}{f_0} \nabla^2 \mathbf{p} - f_0 \underline{\underline{\mathbf{A}}} \mathbf{p}, \qquad (5)$$

where $\mathbf{p} = (p1, p2, p3)$ and $\mathbf{q} = (q1, q2, q3)$ represent the pressure and the QGPV in layers 1–3, $J(A, B) = \partial_x A \partial_y B - \partial_x B \partial_y A$ is the Jacobian operator, and $\mathcal{A}_4 = 2 \times 10^9$ m^2 s^{-1} is the constant biharmonic viscosity. The term $\underline{\underline{\mathbf{A}}}$ is a 3×3 matrix containing the coefficients of the pressures in the η contribution to vorticity, and $\underline{\underline{\mathbf{B}}}$ is a 3×4 matrix containing the inverse

layer thicknesses. Finally, **e** is the entrainment vector which couples the atmospheric Ekman layer, the oceanic surface Ekman layer, and the oceanic bottom Ekman layer to the three layers of the QG model. It is expressed as follows (for the ocean):

$$
\mathbf{e} = \begin{bmatrix} w_{\mathrm{ek}} \\ -\dfrac{T_m - T_1}{2(T_1 - T_2)} w_{\mathrm{ek}} \\ 0 \\ \dfrac{\delta_{\mathrm{ek}}}{2f_0} \nabla^2 p_3 \end{bmatrix}, \tag{6}
$$

with w_{ek} as the Ekman pumping defined in Eq. (3), T_m as the temperature in the surface mixed layer, and T_1 (T_2) as the temperature in the first (second) QG layer.

The temperature difference between two layers and vertical Ekman pumping determine the entrainment heat flux. In our model, the layer's temperature is considered constant and only the mixed layer's temperature is time dependent and inhomogeneous. Vertical heat fluxes which result in the modification of the layer temperature in a specific area are handled through layer stretching: The interface with the upper/lower layer is elevated/lowered over the downwelling/upwelling area, thus locally changing the temperature. The entrainment heat term appearing in the potential vorticity equation is defined only at the interface between the first and second layers:

$$
F_k^{\mathrm{th}} = \pm \frac{f_0}{H_k} \frac{(T_m - T_1)\, w_{\mathrm{ek}}}{T_1 - T_2}, \tag{7}
$$

with H_k as the kth-layer thickness, and this term is defined with a plus sign in the first layer potential vorticity equation and a minus sign in the second layer. The entrainment heat flux through the layer interface influences layer's temperatures according to the sign and amplitude of the vertical velocity. As discussed in the introduction, surface current feedback will modify the curl of the wind stress and thus the induced Ekman pumping [Eq. (3)].

To highlight the impact of relative wind on the oceanic circulation, we run two configurations of the model: one with absolute wind stress formulation following Eq. (2) (referred to as ABS hereafter) and the other with relative wind stress formulation following Eq. (1) (referred to as REL hereafter). In both cases, the simulations are run for 50 years after a common 80-yr spinup, and all the diagnostics are computed over the last 10 years. Although relatively short, the duration of the simulation is sufficient for the model to achieve a quasi-steady state [cf. Fig. 4 of Martin et al. (2020)]. The derivation of the LEC in QG is provided in appendix A for completeness, and some discussion on nonlocality of eddy–mean flow energy transfers is provided in appendix B. Table A1 summarizes the different terms associated in the energy equations. Following Harrison and Robinson (1978), we will refer to potential-to-kinetic energy exchange as energy *conversion*, since the term responsible for it (i.e., wb) is mathematically identical in both kinetic and potential energy equations but with an opposite sign. However, the terms responsible for eddy–mean flow energy exchange are not identical in the

eddy and in the mean equations, where significant nonlocal contributions can be involved when considered regionally (see appendix B). To highlight this difference, we will refer to this type of energy exchange as energy *transfer*, which formally represents the energetic signature of eddy–mean flow interactions. In keeping with notation in Jamet et al. (2022), we will use the shorthand "MEC" to refer to the terms associated with the mean equations and the shorthand "EF" to refer to the terms associated with the eddy equations. For the potential energy equations, these terms will read P_MEC and P_EF, and for the kinetic energy equations, they are kinetic mean-to-eddy conversion (K_MEC) and kinetic eddy flux (K_EF). We will also perform wavenumber spectral analysis of relevant terms in order to assess the energy distribution and fluxes as a function of spatial scale. Details are provided in appendix C (also see, e.g., Capet et al. 2008; Arbic et al. 2013, for consistency). We simply recall here that a positive (negative) slope in spectral fluxes is associated with a sink (source) of energy within the associated wave band and that the basin-scale estimate (smallest wavenumber) reflects the values reported in the LEC (Fig. 1).

3. Mechanical and thermodynamical ocean surface fluxes

Figure 1 synthesizes the content of the four energy reservoirs along with the associated exchanges and the forcing and dissipative energy fluxes for the two simulations ABS and REL. Absolute values are given for ABS, and relative differences observed in REL are expressed in % (see caption for details). In both cases, the external forcing terms responsible for energy exchanges with the atmosphere are the diabatic heating and the wind stress forcing (top and bottom arrows), driving potential and kinetic energy, respectively. Bottom friction and viscous dissipation represent the internal processes resulting in a drain of kinetic energy (right arrows).

This diagram exhibits the hierarchy between energy reservoirs traditionally diagnosed in geophysical flows (Vallis 2006): The mean PE (MPE) level is the largest and then comes the EKE, the EPE, and the mean KE (MKE). More than 80% of the total energy of the ocean is stored in the potential energy of the mean flow. This means that nearly all of the mean ocean energy is present as buoyancy anomaly (potential energy) rather than transport (kinetic energy). For the eddy field, there is roughly an equipartition between EKE and EPE, as expected from QG theory.

Comparing ABS and REL first reveals that the most important contribution of relative wind stress formulation is to change the sign of turbulent wind work and turbulent diabatic heating (i.e., turbulent surface forcing; bottom black and red arrows). In the ABS simulation (numbers in black), the turbulent wind work provides energy to the EKE at a rate of +3 GW and the turbulent diabatic heating provides energy to the EPE at a rate of +1 GW. In contrast in the REL simulation (numbers in blue), the turbulent wind work extracts energy from the EKE at a rate of −11 GW and the turbulent diabatic heating extracts energy from the EPE at a rate of −5 GW. The global energy balance is also significantly modified, with a reduction of about 20% in energy input and dissipation.
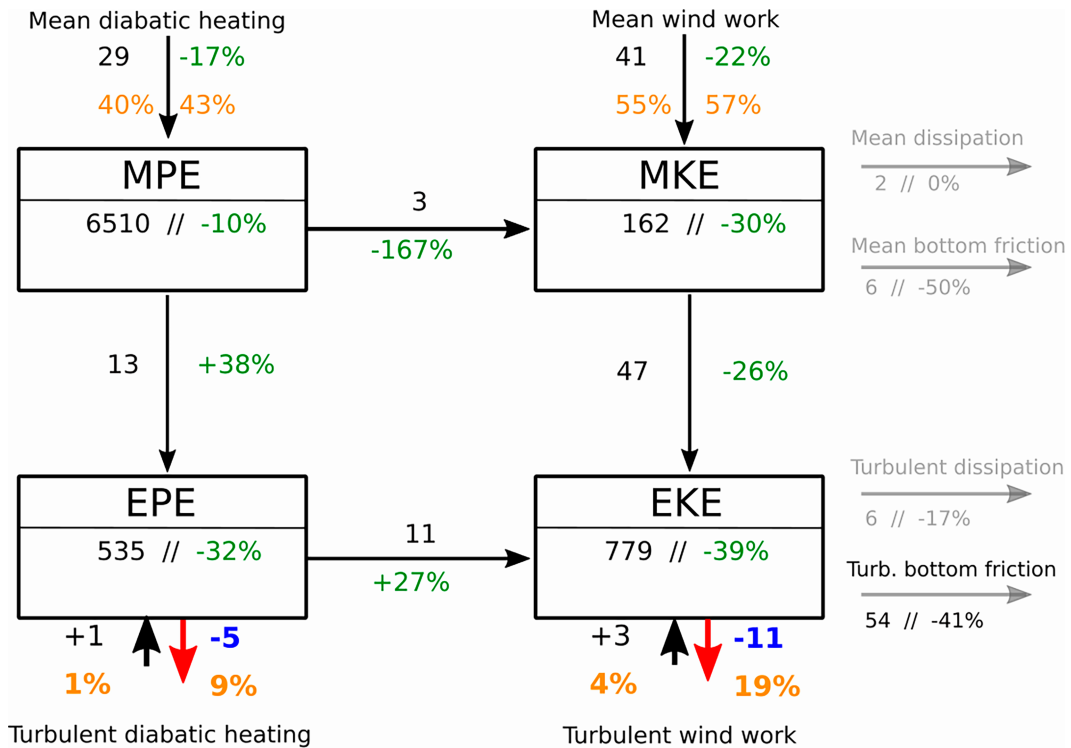
FIG. 1. LEC for both simulations. Results for the absolute wind stress scenario (ABS) are shown in black, and the relative differences for the relative wind stress scenario (REL) are shown in green and expressed in percentage. For turbulent diabatic heating and wind work, energy fluxes for REL are reported in blue in order to highlight their changes in sign and magnitude. The relative contribution (%) of wind work and diabatic heating for the total energy input/dissipation are also shown in orange. Units are in petajoule (1 PJ = 10^{15} J) and gigawatts (1 GW = 10^9 W) for energy content and fluxes, respectively.

The relative contributions of turbulent wind work and turbulent diabatic heating to the total energy balance thus jump from 4% and 1% in ABS, respectively, to 19% and 9% in REL, in agreement with recent estimates (Zhu et al. 2023). The wind stress formulation thus has two main contributions in how the ocean and atmosphere components of the Q-GCM interact through eddies.

First, the relative wind stress formulation strongly increases the relative contribution of both air–sea turbulent fluxes by about one order of magnitude in the global energy balance, a result of both a reduced total energy balance and a significant amplification of the turbulent wind work and turbulent diabatic heating. Second, the relative wind stress formulation reverts surface eddy fluxes from a source to a sink of eddy energy. The contribution of these turbulent fluxes is mostly confined within the jet region (Fig. 2), where most of the ocean turbulence is observed. Turbulent wind work is characterized by positively skewed eddy-size structures in ABS, leading to a net positive contribution (i.e., a source of EKE) over the full domain. This eddying structure changes radically into a broad and homogeneous negative structure (i.e., a sink of EKE) along the jet in REL, with residual positive contributions in the ocean interior. Such a change is consistent with the *eddy killing* effects observed by Renault et al. (2016) in their realistic simulations of the North Atlantic simulations (cf. their Fig. 7). Similar results are found for the turbulent

diabatic heating (Fig. 2, bottom panels), which is also characterized by positively skewed eddy-size structures in ABS (i.e., a source of EPE), but by a homogeneous negative contribution in REL (i.e., a sink of EPE). The contribution of relative wind formulation on turbulent diabatic heating is to induce a turbulent Ekman pumping driving heat flux between the Ekman layer and the upper QG layer. As sketched in Fig. 3, cyclonic eddies are associated with a downwelling at the base of the Ekman layer, inducing a downward heat flux within the upper layer T_1, thus damping the negative heat anomaly associated with cyclonic eddies. The opposite is true for anticyclonic eddies, where relative wind stress induces an additional upwelling, extracting part of their positive heat anomaly. For a well-defined eddy, this transport will always reduce heat anomalies, damping the eddy, and thus its associated potential energy.

Turbulent diabatic heating can be further decomposed into a contribution associated with time mean and time-varying mixed layer temperature T_m (Fig. 4). This decomposition reveals turbulent diabatic heating is largely driven by turbulent Ekman pumping acting on the time mean mixed layer temperature, while the contribution of time variations of T_m plays a secondary, although nonnegligible, role. This result further supports our previous interpretation which neglects the response of the oceanic mixed layer temperature to the induced heat fluxes associated with Ekman pumping. We note, however,
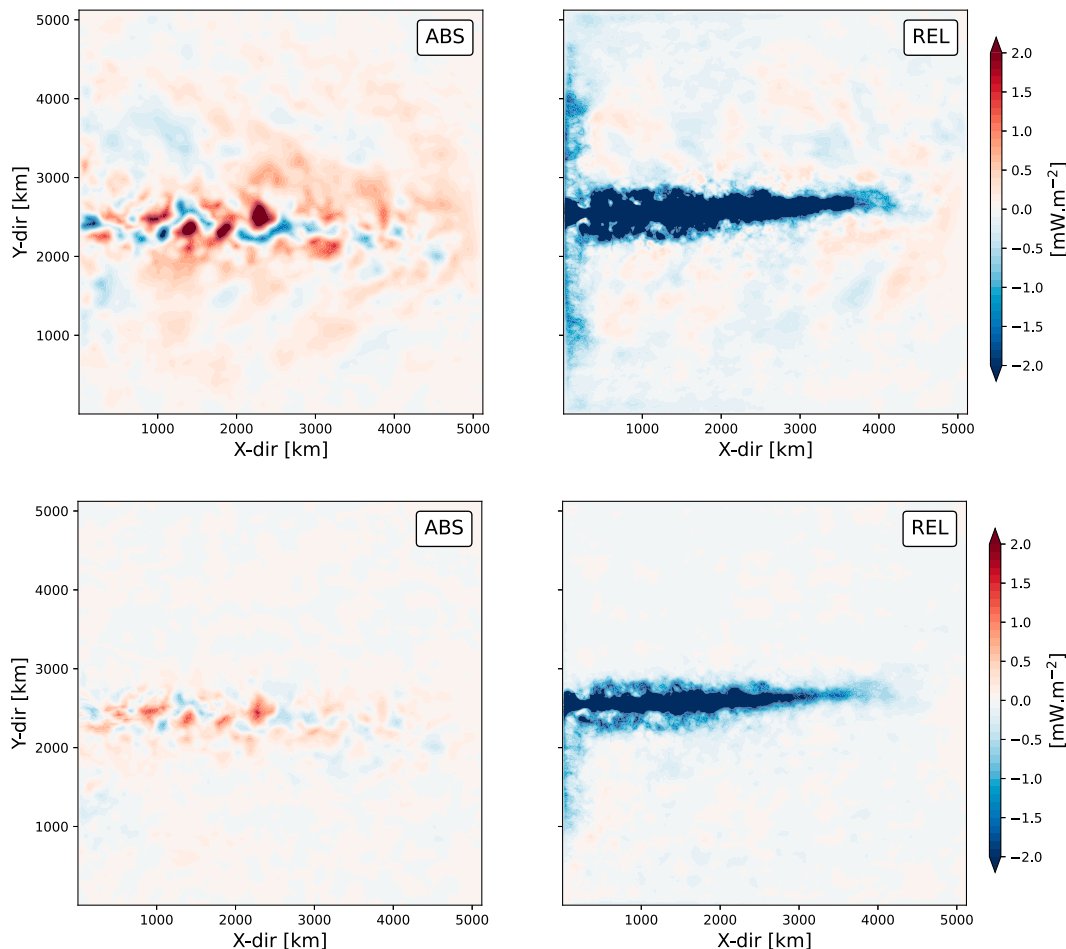
FIG. 2. (top) Turbulent wind work and (bottom) turbulent diabatic heating for (left) the absolute simulation and (right) the relative simulation (see text, appendix A, and Table A1 for further details of these terms).

that in Q-GCM, air–sea heat fluxes are computed with a restoring strategy and do not account for relative wind stress formulation in these types of fluxes which may well impact the temperature of the oceanic mixed layer. Further analyses would be required to evaluate such a contribution for ocean energetics, but they are outside of the scope of the present paper.

Finally, we note that the budgets are not close to machine precision, with sources and sinks of total energy that do not perfectly balance, reflecting a rate of change in the different energy reservoirs. These residuals are relatively weak (<10% for ABS and <5% for REL) and may be due to the relatively short period used for the analysis (10 years) and to the relatively coarse temporal resolution we used for saving model outputs (15-day averages). Another potential source of uncertainty lies in the eddy rectification term, which has been shown to converge very slowly [$\sim\mathcal{O}(10^4)$ years; Uchida et al. 2022], contaminating the quality of the steady-state statistics. However, we do not anticipate such convergence issue to significantly modify our estimates of the time mean flow structure as the system reaches a nearly steady state after only 10 years of spinup (Martin et al. 2020). Especially, we have verified that the meridional extension of the oscillating mean jet is a robust

feature of the experiments and does not reflect a transitional state induced by a lack of convergence (not shown). This last point is of particular interest for the discussion in section 4b, where we interpret the reduction in eddy–mean flow energy transfers in REL as a result of a more stable jet with less pronounced meanders. We do not expect such an interpretation to be biased by this potential convergence issue.

4. Energy exchanges

We now turn our attention to the modifications induced by a change from absolute to relative wind stress formulation for the exchanges between the different energy reservoirs. We focus here on the potential-to-kinetic eddy energy conversion and on the eddy–mean flow potential energy transfers.

a. Potential-to-kinetic eddy energy conversion

As shown in Fig. 1, potential-to-kinetic eddy energy conversion $\overline{w'b'}$ is +27% larger in REL. From the spatial distribution of energy conversion $\overline{w'b'}$ (Fig. 5), the net increase in energy conversion does not appear as an obvious signature, since both potential-to-kinetic (positive values) and kinetic-to-potential
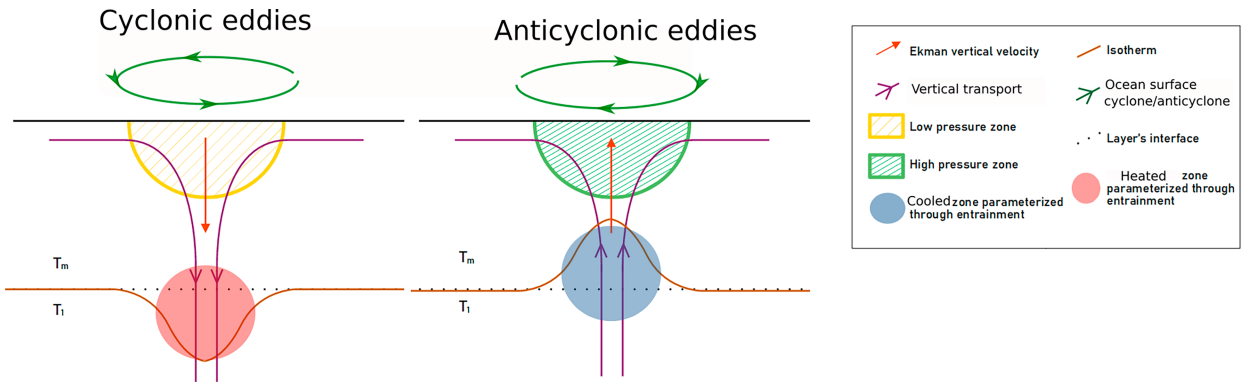
FIG. 3. Schematic of the process resulting in Ekman pumping, for (left) cyclonic eddies and (right) anticyclonic eddies in the Northern Hemisphere. The terms T_m and T_1 refer to the temperature in the ocean surface mixed layer and in the ocean first QG layer, respectively.

(negative values) energy conversions exhibit small differences between ABS and REL. It is their net, averaged effects that result in a +27% increase, indicative of a larger increase in potential-to-kinetic turbulent energy conversion. Spectral fluxes of energy between EPE and EKE (Fig. 5, bottom panel) provide a complementary view. We recover the net +27% at the largest scale (smallest k), in agreement with the relative wind-induced Ekman pumping anomaly due to absolute forcing (investigated by Gaube et al. 2015). However, the net increase is not uniformly distributed across scales, where we rather observe a significant reduction at most wavenumbers. That the net (basin-scale estimates) spectral fluxes are larger in REL than in ABS is a consequence of a stronger reduction in EKE to EPE (positive slope) at low wavenumber than in EPE to EKE (negative slope) at high wavenumber. Thus, in the general energy cycle associated with baroclinic instability, where EPE is expected to be transferred toward EKE in order to be dissipated, this may well suggest that relative wind stress favors scales associated with energy conversion needed to reach dissipative scales and thus an energetically balanced state.

b. Eddy–mean flow energy transfers

Finally, we quantify the imprints of the relative wind stress formulation on the energy transfers between the mean and the turbulent flow. For KE, those transfers are usually related to barotropic instabilities: Jamet et al. (2021) showed that at leading order in the Gulf Stream, this MKE-to-EKE transfer roughly balances the net mean wind work over the North Atlantic subtropical gyre. Here, we pay a particular attention to the eddy–mean flow transfers of potential energy as those show a +38% increase in REL, which questions the underlying dynamics given both MPE and EPE have decreased by −10% and −32%, respectively. In contrast, eddy–mean flow transfers of kinetic energy are weakened by −26%, following the reduction in MKE and EKE of about the same amplitude (cf Fig. 1) and consistent with Renault et al. (2019).

We show in Fig. 6 the spectral fluxes of P_MEC for ABS and REL. In both runs, spectral fluxes reveal that MPE feeds EPE (i.e., positive slope) between 200 and 1250 km ($k = 5 \times 10^{-3}$–8×10^{-4} cpkm, respectively), a wave band corresponding to mesoscale turbulence suggesting mesoscale eddy generation processes. This is a typical signature of a forward energy cascade. At larger scales (1250–2500 km; $k = 8 - 4 \times 10^{-4}$ cpkm), spectral fluxes indicate a transfer from eddy to mean potential energy (i.e., negative slope), indicative of a noticeable backscattering energy contribution which is likely associated with the absorption of eddies by the mean flow. This is a typical signature of an inverse energy cascade. By
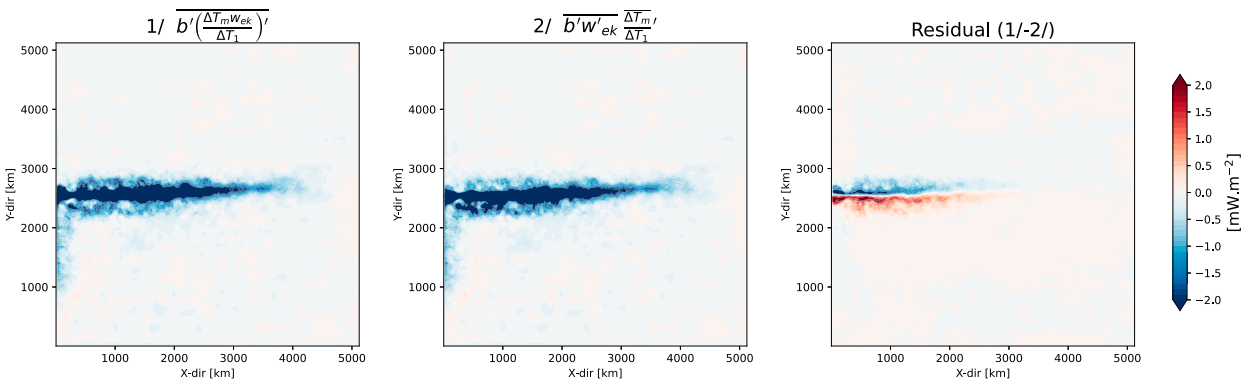

FIG. 4. (left) Total turbulent diabatic heating in REL, decomposed into a contribution driven by (center) time mean mixed layer temperature T_m and (right) T_m anomalies (computed as a residual).
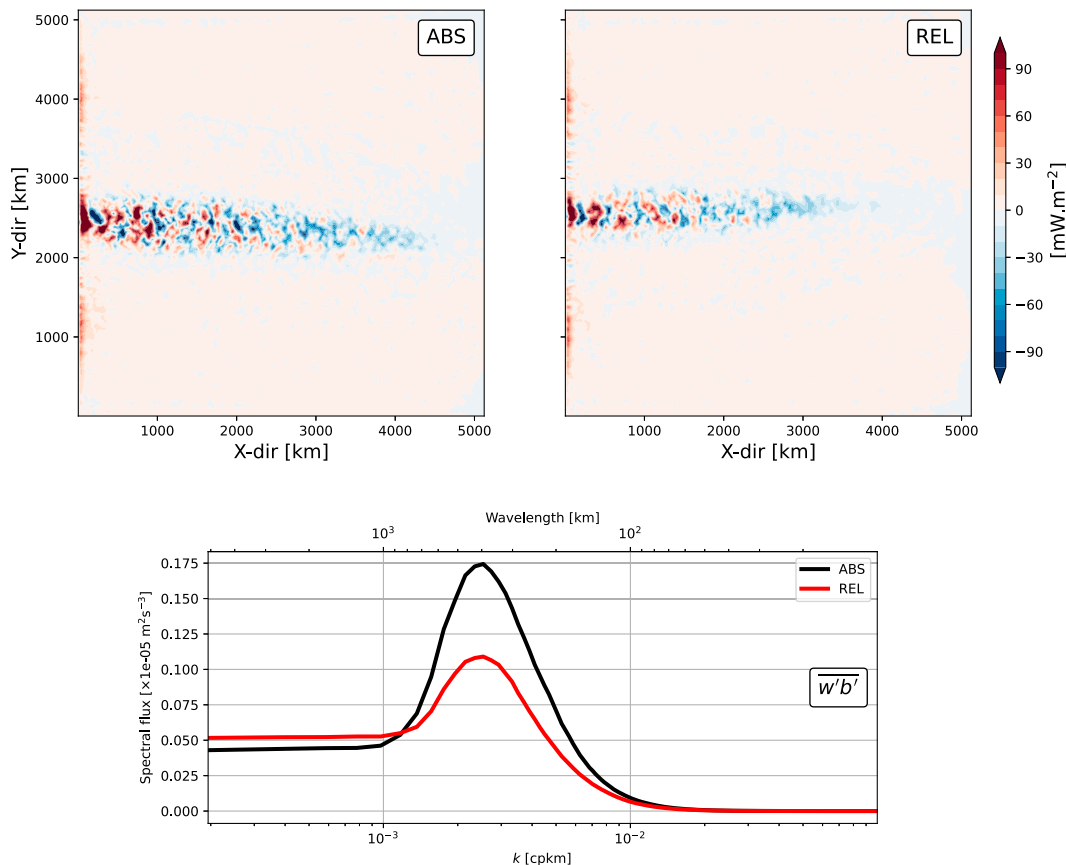
FIG. 5. (top) Spatial distribution of energy conversion between the turbulent potential and turbulent KE $\overline{w'b'}$ for (left) the absolute simulation and (right) the relative simulation. Red (blue) regions are associated with a conversion from potential (kinetic) to kinetic (potential) turbulent energy. (bottom) Spectral fluxes of energy conversion between the EPE and the EKE $\overline{w'b'}$, where a positive slope is associated with a conversion from EKE to EPE and a negative slope is associated with a conversion from EPE to EKE. Net EPE–EKE conversion, as reported in Fig. 1, is associated with the value at the smallest k (i.e., leftmost values).

comparing the two simulations, it appears that at nearly all scales shorter than 2500 km ($k > 4 \times 10^{-4}$ cpkm), P_MEC spectral fluxes are weaker in REL than in ABS. Specifically, relative wind forcing yields a less vigorous forward cascade at small scales (positive slopes for $k > 8 \times 10^{-4}$ cpkm), but more importantly, a very strong reduction in the inverse cascade at scales between 1250 and 2500 km ($k = 8$–4×10^{-4} cpkm) suggesting a significant weakening of the energy backscattering mechanism. A more pronounced forward cascade completes the picture at basin scale in REL, which is responsible for the net +38% increase in P_MEC reported in Fig. 1. Our results thus extend the recent results of Renault et al. (2019) to potential energy. They observed a reduction in both forward and inverse cascades of kinetic energy spectral fluxes in realistic coupled simulations of the Gulf Stream and the Agulhas Current, with a stronger reduction in the inverse cascade (30%–40%) as compared to the reduction in the forward cascade (10%–20%).

To help our interpretation of the dynamics driving these eddy–mean flow potential energy transfers, we show in Fig. 7 the depth-integrated P_MEC contribution for which spectral fluxes have been computed, as well as their EPE equivalent

P_EF in Fig. 8. Indeed, to fully appreciate the spatial organization of energy transfers between mean and turbulent energy reservoirs, it has recently been shown by several studies that nonlocal energy transfers need to be considered (Chen et al. 2014; Kang and Curchitser 2015; Matsuta and Masumoto 2021; Jamet et al. 2022). Nonlocal processes reflect the fact that energy lost by the mean flow at one location can be transported over significant distances before to be either reinjected within the mean flow or sustained by the growth of the turbulent flow. Formally, this can be explained through the divergence of a turbulent flux of cross-energy terms (see appendix B for further details). Comparing the spatial organization of P_MEC and P_EF (Figs. 7 and 8, respectively) provides a measure of such nonlocality. Although in both ABS and REL differences are significant, we nonetheless point out that both P_MEC and P_EF exhibit some degree of spatial correlation between regions of negative P_MEC and regions of positive P_EF, as, for example, right at the western boundary where the jet detaches. The spatial organization of P_MEC and P_EF thus suggests nonlocal dynamics may not be a leading-order contribution along the jet in our setup. This represents a noticeable
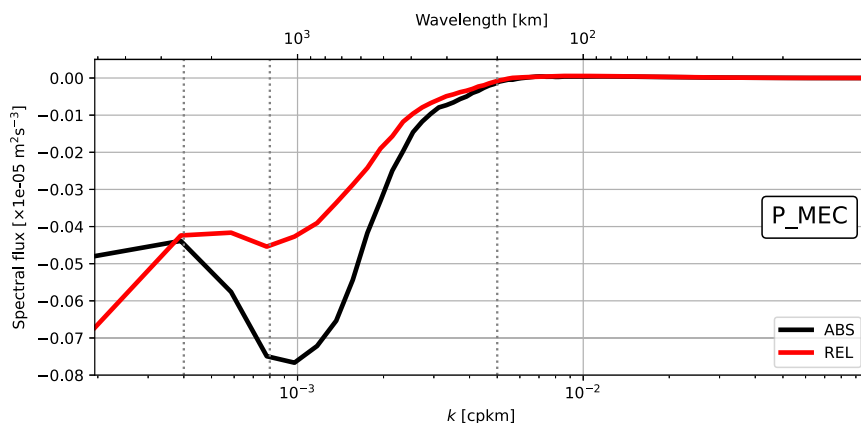
FIG. 6. Spectral fluxes of eddy–mean flow PE transfers (P_MEC). Positive slopes are associated with transfers from MPE to EPE (i.e., forward cascade of energy), and negative slopes are associated with energy transfers from EPE to MPE (i.e., inverse cascade of energy). Dotted vertical lines correspond to wavelengths 2500, 1250, and 200 km referred in the text.

difference with results from previous studies based on realistic, primitive equation models where nonlocality has been found to be significant in eddy regions (i.e., western boundary currents and Antarctic Circumpolar Current; e.g., Chen et al. 2014). Further analyses are required to evaluate whether this is specific to our idealized setting or whether it is a consequence expected under quasigeostrophy. We still note one major difference between P_MEC and P_EF associated with their respective magnitudes along the jet: While P_EF is maximum at the center of the jet, P_MEC has a local minimum. This can be explained by the dynamics behind these transfers: P_EF is associated with horizontal gradients of the mean buoyancy field $\nabla \overline{b}$, which are largest at the center of the jet; on the other hand, P_MEC is associated with mean buoyancy field $\overline{b}$, which is associated with a local minimum along the jet. It is of interest to note that the spatial organization of P_EF shares

some similarities with K_MEC (discussed in Jamet et al. 2022, but for primitive equations, realistic models), while the spatial organization of P_MEC shares some similarities with K_EF.

We now focus on the spatial organization of P_EF along the jet in ABS (Fig. 8, bottom left panel). Comparing the meanders of the time mean jet, represented by the orange contour (cf caption), with the location of EPE sources and sinks, we can see that red (blue) regions are colocalized with the parts of the meanders that move away (toward) the jet mean latitude (represented with a white line). The spatial organization of P_EF with the meandering mean jet suggests preferred dynamical regions for eddy generation (red spots) and eddy backscattering (blue spot) depending on the meridional excursion of the mean jet. Given that the time mean jet in REL exhibits a much weaker meandering structure (Fig. 8, bottom right panel), this may well provide a dynamical rationalization to interpret the
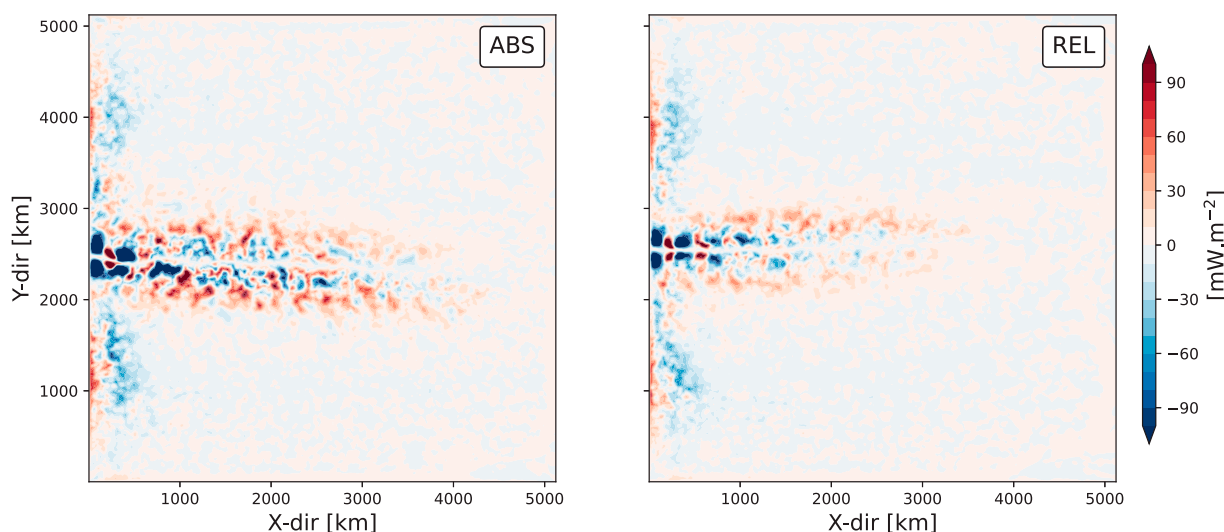

FIG. 7. Depth-integrated contribution of P_MEC for the (left) absolute wind stress simulation and (right) relative wind stress simulation. Red shading indicates a local source of MPE. The basin-integrated contribution is a sink of MPE of about −13 (−18) GW for ABS (REL; see Fig. 1).
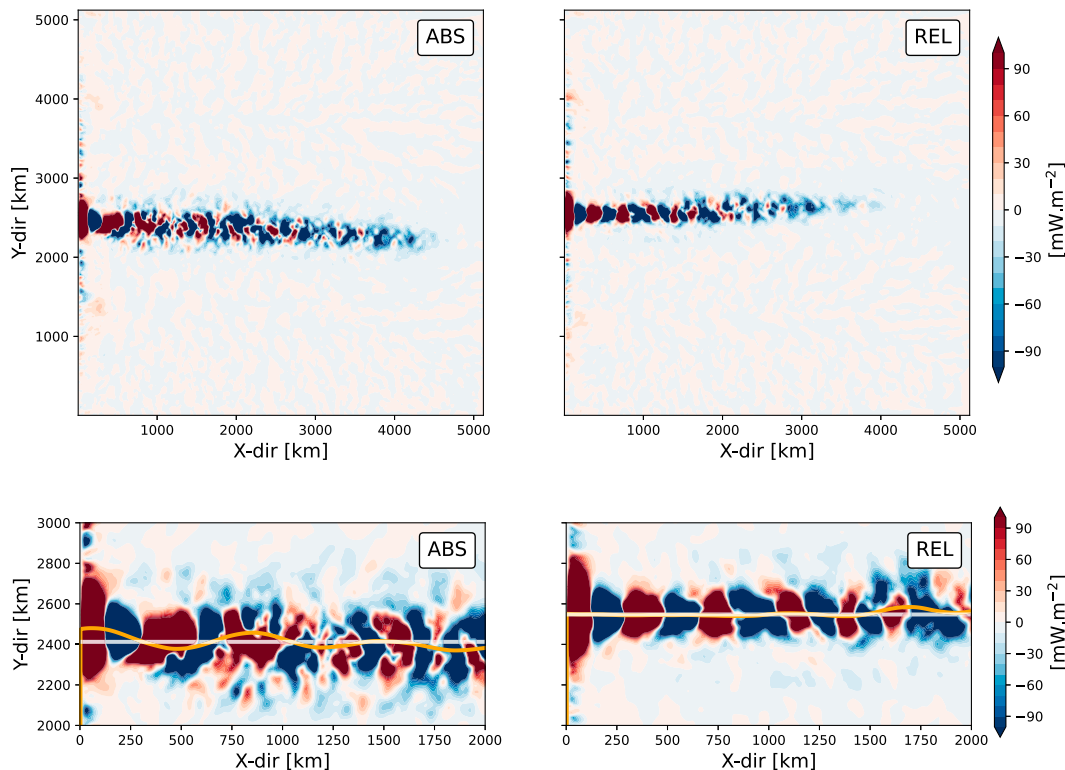
FIG. 8. (top) Depth-integrated contribution of P_EF for the (left) absolute run and (right) relative run. Red shading indicates a local source of EPE. (bottom) A zoom on the jet region showing the spatial organization of P_EF relative to the time mean zero mean streamfunction $\overline{\psi}$ in the first layer (orange contour). The white line indicates the meridional position of the zonally averaged time mean zero mean streamfunction 2000 km away from the western boundary.

strong reduction in inverse energy cascade observed in REL. This statement, however, remains speculative and is discussed here only to provide potential directions for further studies.

5. Conclusions and discussion

In this study, we have investigated the impact of the relative versus absolute wind stress formulation on the ocean energy reservoirs and exchanges in the context of Lorenz energy cycles (LECs). We have conducted this analysis with an idealized, quasigeostrophic coupled model (Q-GCM; Hogg et al. 2006), where a 3-layer QG ocean model interacts with a 3-layer QG atmospheric model through Ekman layers. The main contribution of our study is to provide evidence of the thermodynamical impact of ocean current feedback on the energetics of the ocean via Ekman pumping. Through this effect, both upscale and downscale transfers of energy between mean and eddy potential energy, as well as energy conversion between the potential and kinetic energy of the eddies, are strongly reduced. However, upscale transfers are more reduced than downscale transfers, resulting in a net increase in energy transfers (see Fig. 1). The reduced upscale transfer we observe in response to surface current feedback is consistent with what Renault et al. (2019) observed in realistic regional simulations and satellite observations in the Gulf Stream and the Agulhas Current region for kinetic energy spectral fluxes.

To our knowledge, spatial patterns and induced changes in energy transfers associated with the thermodynamical feedback have not been reported by others based on realistic simulations nor observations. Nonetheless, both mechanical (*eddy killing*) and thermodynamical (Ekman pumping) ocean current feedbacks have the expected behavior on a basin-averaged sense (Dewar and Flierl 1987; Gaube et al. 2015). We note that the relative impact of surface current feedback we have reported on here is to be interpreted cautiously for applications to realistic ocean models or observations. Indeed, we have conducted our analysis with an idealized model where only three layers are used in the vertical, while ocean surface current feedback is well confined within the upper 30–50 m of the ocean in realistic conditions (Ma et al. 2016). Our results thus provide a first step in this direction, in the context of QG dynamics, and should be further validated.

Comparing the horizontal structures of eddy–mean flow energy transfers, we highlighted the opposite behavior between kinetic and potential energy. For kinetic energy, production or destruction of MKE through K_MEC is larger along the jet, while its associated EKE component, K_EF, is larger on the flanks of the jet, an organization largely driven by the horizontal structure of the mean flow and that of its gradients, respectively (see Jamet et al. 2022, for broader discussion). Our results suggest that a similar argument can be made for potential energy but with an opposite structure, namely, that production or destruction of MPE

through P_MEC is larger on the flanks of the stream and its associated EPE component, P_EF, is larger along the jet. This may well suggest that similar dynamical constraints, as reported by Jamet et al. (2022), could be relevant to better understand how the mean flow and the eddy dynamics exchange their energy and thus reach an energetically balanced state. Given that nonlocal eddy–mean flow energy transfers have been found to be of larger magnitude for the potential energy than for the kinetic energy by Chen et al. (2014), it would be of interest to further study such potential dynamical constraints in the context of potential energy.

Data availability statement. Lorenz energy cycles and associated vertically integrated maps and spectral fluxes have been computed with the qgutils Python packages (https://zenodo.org/badge/latestdoi/612190785). The Q-GCM parameters, along with Python scripts used to produce results discussed here, are available at https://zenodo.org/badge/latestdoi/258128829.

APPENDIX A

Lorenz Energy Cycle in Quasigeostrophic Models

The Lorenz energy cycle (LEC), originally formulated for the atmosphere by Lorenz (1955) and subsequently adapted

to the ocean (Harrison and Robinson 1978; Oort et al. 1994), provides a descriptive understanding of the different energy reservoirs of a Boussinesq, incompressible fluid (ocean or atmosphere) partitioned into four quantities usually referred to as mean potential energy (MPE) and mean kinetic energy (MKE) and its eddy counterpart (EPE and EKE). Analysis of the LEC allows to identify leading-order energetic contributions for the ocean circulation, as well as the myriad of interactions between the different reservoirs and the external forcings (momentum and buoyancy fluxes and boundary contribution in the case of a regional analysis).

The time evolution of the QG potential vorticity equation is defined as (ignoring forcing and dissipation for simplicity)

$$\partial_t q + \mathbf{u}_g \cdot \nabla_h q = 0, \tag{A1}$$

with the $\mathbf{u}_g$ as the geostrophic velocities and

$$q = \Delta\psi + \beta(y - y_0) + \partial_z\left(\frac{f_0^2}{N^2}\partial_z\psi\right), \tag{A2}$$

the QG potential vorticity, defined based on the streamfunction $\psi = p/\rho_0 f_0$, where p is the pressure, ρ_0 is the reference density, and f_0 is the reference Coriolis frequency used in the β-plane approximation $f = f_0 + \beta(y - y_0)$. Equation (A1) provides a single evolution equation constructed based on the momentum and the continuity equations for an incompressible, Boussinesq fluid subject to geostrophic approximations, i.e.,

$$\partial_t(\Delta\psi) = -J(\psi, \Delta\psi) + f_0\partial_z w, \tag{A3}$$

for the momentum equation and

TABLE A1. Table explaining the physical meaning for each term present in energy equations. Bold text in the right column refers to the abbreviations used throughout this paper to refer to eddy–mean flow energy transfers. Although we abusively refer to a *conversion* of energy in the shorthand MEC, this choice is made to keep with the notation proposed by Jamet et al. (2021, 2022). Buoyancy b is defined here as $b = f_0\partial_z\psi$.

Reservoir	Mathematical expression	Physical interpretation
MKE	$\overline{\psi J(\overline{\psi}, \Delta\overline{\psi})}$	MKE advection
	$\overline{\psi J(\psi', \Delta\psi')}$	Energy exchanges with the EKE (**K_MEC**)
	$\overline{w}\,\overline{b}$	Energy conversion with the MPE
	$-f_0\,\overline{\psi w_{\text{ek}}}$	Mean wind work
EKE	$\overline{\psi' J(\psi', \Delta\overline{\psi})}$	Energy exchanges with the MKE (**K_EF**)
	$\overline{\psi' J(\psi, \Delta\psi')}$	EKE advection (by both the mean and the turbulent flow)
	$\overline{w'b'}$	Energy conversion with the EPE
	$-f_0\,\overline{\psi' w'_{\text{ek}}}$	Turbulent wind work
MPE	$-\dfrac{1}{N^2}\,\overline{b J(\overline{\psi}, \overline{b})}$	MPE advection
	$-\dfrac{1}{N^2}\,\overline{b J(\psi', b')}$	Energy exchanges with the EPE (**P_MEC**)
	$-\overline{w}\,\overline{b}$	Energy conversion with the MKE
	$\overline{b\left(\dfrac{\Delta T_m w_{\text{ek}}}{\Delta T_1}\right)}$	Mean diabatic heating
EPE	$-\dfrac{1}{N^2}\,\overline{b' J(\psi', \overline{b})}$	Energy exchanges with the MPE (**P_EF**)
	$-\dfrac{1}{N^2}\,\overline{b' J(\psi, b')}$	EPE advection (by both the mean and the turbulent flow)
	$-\overline{w'b'}$	Energy conversion with the EKE
	$\overline{b'\left(\dfrac{\Delta T_m w_{\text{ek}}}{\Delta T_1}\right)'}$	Turbulent diabatic heating

$$f_0 \partial_t (\partial_z \psi) = -f_0 J(\psi, \partial_z \psi) - N^2 w, \qquad (A4)$$

for the buoyancy equation (buoyancy is here defined as $b = f_0 \partial_z \psi$), where $J(A, B) = \partial_x A \partial_y B - \partial_x B \partial_y A$ is the Jacobian operator, $\Delta = \nabla^2 = \partial_x^2 + \partial_y^2$ is the Laplacian operator, and w is the ageostrophic, small amplitude vertical velocity. Equations of evolution for the kinetic energy,

$$KE = \frac{1}{2}(\nabla \psi \cdot \nabla \psi), \qquad (A5)$$

and for the potential energy,

$$PE = \frac{1}{2}\left[\frac{f_0^2}{N^2}(\partial_z \psi)^2 \right], \qquad (A6)$$

are then obtained by multiplying Eq. (A3) by $-\psi$ and Eq. (A4) by $(f_0/N^2)\partial_z \psi$, respectively. Volume-integrated kinetic and potential energy equations read

$$\int_\Omega \partial_t KE \, dV = \int_\Omega \psi J(\psi, \Delta \psi) \, dV - \int_\Omega f_0 \psi \partial_z w \, dV, \qquad (A7)$$

and

$$\int_\Omega \partial_t PE \, dV = -\int_\Omega \frac{f_0^2}{N^2} \partial_z \psi J(\psi, \partial_z \psi) dV - \int_\Omega f_0 \partial_z \psi \, w \, dV, \qquad (A8)$$

where Ω is the full domain.

We now introduce the Reynolds decomposition:

$$X = \overline{X} + X', \qquad (A9)$$

with $\overline{X}$ as a time averaging. We apply this decomposition to Eqs. (A7) and (A8) to get the eddy kinetic energy and potential energy (EKE $= \overline{KE'}$ and EPE $= \overline{PE'}$) and the mean kinetic energy and potential energy (MKE $= \overline{\overline{KE}}$ and MPE $= \overline{\overline{PE}}$):

$$\int \partial_t \overline{\overline{KE}} \, dV = \int \left[\overline{\psi} J(\overline{\psi}, \Delta \overline{\psi}) + \overline{\psi} \, \overline{J(\psi', \Delta \psi')} \underbrace{- f_0 \overline{\psi} \partial_z \overline{w}}_{= \overline{w}\overline{b}} - \frac{\delta_E f_0}{2H_2} \overline{\psi} \Delta \overline{\psi} - f_0 \overline{\psi} \overline{w}_{ek} \right] dV, \qquad (A10)$$

$$\int \partial_t \overline{KE'} \, dV = \int \left[\overline{\psi' J(\psi', \Delta \overline{\psi})} + \overline{\psi' J(\overline{\psi}, \Delta \psi')} + \overline{\psi' J(\psi', \Delta \psi')} \underbrace{- f_0 \overline{\psi' \partial_z w'}}_{= \overline{w'b'}} - \frac{\delta_E f_0}{2H_2} \overline{\psi' \Delta \psi'} - f_0 \overline{\psi' w'_{ek}} \right] dV, \qquad (A11)$$

$$\int \partial_t \overline{\overline{PE}} \, dV = \int \left[-\frac{f_0^2}{N^2} \overline{\partial_z \psi} J(\overline{\psi}, \overline{\partial_z \psi}) - \frac{f_0^2}{N^2} \partial_z \overline{\psi} \, \overline{J(\psi', \partial_z \psi')} \underbrace{- f_0 \partial_z \overline{\psi} \, \overline{w}}_{= -\overline{w}\overline{b}} + f_0 \partial_z \overline{\psi} \, \overline{\left(\frac{\Delta T_m w_{ek}}{\Delta T_1} \right)} \right] dV, \qquad (A12)$$

$$\int \partial_t \overline{PE'} \, dV = \int \left[-\frac{f_0^2}{N^2} \overline{\partial_z \psi' J(\psi', \partial_z \overline{\psi})} - \frac{f_0^2}{N^2} \overline{\partial_z \psi' J(\overline{\psi}, \partial_z \psi')} - \frac{f_0^2}{N^2} \overline{\partial_z \psi' J(\psi', \partial_z \psi')} \underbrace{- f_0 \overline{\partial_z \psi' w'}}_{= -\overline{w'b'}} + f_0 \partial_z \psi' \overline{\left(\frac{\Delta T_m w_{ek}}{\Delta T_1} \right)'} \right] dV. \qquad (A13)$$

Dynamical interpretations of the terms in Eqs. (A10)–(A13) are provided in Table A1. In this paper, we will focus on the terms of transfers of energy between the four reservoirs and analyze their sensitivity to wind stress formulation and their nonlocality.

APPENDIX B

Nonlocal Energy Transfers in Quasigeostrophic Models

Following previous studies (e.g., Harrison and Robinson 1978; Chen et al. 2014), we will refer to local processes when the energy lost by the mean flow sustains *locally* the growth of perturbations (or vice versa in the case of back-scattering). If the energy lost by the mean flow at one location does not sustain the growth of eddies at that location

but is exported away, we will refer to it as *nonlocal* processes. This can be formally understood as the degree of compensation between the two terms of eddy–mean flow interaction in both the mean and eddy energy equations, which are not mathematically the same but are linked through the divergence of a turbulent flux of eddy–mean flow interaction term. For the case of the potential energy, this reads

$$\underbrace{\overline{b \, J(\psi', b')}}_{A} = \underbrace{\overline{J(\psi', \overline{b}b')}}_{B} - \underbrace{\overline{b' J(\psi', \overline{b})}}_{C}, \qquad (B1)$$

where A appears in the MPE equation, C appears in the EPE equation, and B is the *nonlocal* term. The degree of locality can be estimated based on the magnitude of the divergent term $\overline{J(\psi', \overline{b}b')}$: Transfers are local when this term

is small and nonlocal when it is leading order. A similar derivation can be made for the kinetic energy, leading to similar conclusions. We note, however, that when using the vorticity–streamfunction form of the QG equations, as in the present manuscript, this derivation involves several integration by part. An alternative would be to use the momentum–buoyancy form of QG equations, as in, e.g., Roullet et al. (2012), but we have not considered it here since our focus is on potential energy. We note that integrated over the full domain subject to no flux boundary conditions, these *nonlocal* terms are identically zero and do not contribute in the LEC of Fig. 1 and discussed in section 3.

Hereafter, we will work with depth-integrated energy exchanges. The conversion from potential energy to kinetic energy (or vice versa) is then exact and expressed as wb. This can be seen by integrating by part (on the vertical) the last term on the rhs of the KE equation [Eq. (A7)]:

$$\int f_0 \psi \partial_z w \, dz = [f_0 \partial_z (\psi w)]_{z=H}^{z=0} - \int w f_0 \partial_z \psi \, dz = -\int wb \, dz,$$
(B2)

with buoyancy $b = f_0 \partial_z \psi$ and where homogeneous surface and bottom (i.e., $w|_{z=\eta, z=H} = b|_{z=\eta, z=H} = 0$) boundary conditions have been considered for the divergent term. We exactly recover the production term for the PE equation [Eq. (A8)].

APPENDIX C

Spectral Analysis

Finally, we will evaluate the wavenumber domain spectral distribution of energy reservoirs as well as their associated spectral energy fluxes. The different terms derived in the physical space in appendixes A and B are transposed in spectral space as follows. We will first consider the kinetic energy by considering the material derivative of relative vorticity. As such, we will not write the terms representing the energy losses and gains because they can be treated just as will be treated the advection term in the following demonstration. An expression with all the terms written will be mentioned later.

$$\frac{D\zeta}{Dt} = \frac{\partial \zeta}{\partial t} + u \nabla \zeta.$$
(C1)

We first carry out a discrete Fourier transform on our equation, noting $A = u \nabla \zeta$:

$$\frac{\partial \zeta}{\partial t} + A = \sum_{\mathbf{k}} \frac{\partial}{\partial t} \widehat{\zeta_k} \, e^{i\mathbf{k}\cdot\mathbf{x}} + \sum_{\mathbf{k}} \widehat{A_k} \, e^{i\mathbf{k}\cdot\mathbf{x}}.$$
(C2)

To obtain the time derivative of the kinetic energy at one wavenumber, we multiply the above equation by the complex conjugate of the discrete Fourier transform of ψ at the

wavenumber r [similar to what we did to go from Eqs. (A3) to (A7)]:

$$\psi \left(\sum_{\mathbf{k}} \frac{\partial}{\partial t} \widehat{\zeta_k} \, e^{i\mathbf{k}\cdot\mathbf{x}} + \sum_{\mathbf{k}} \widehat{A_k} \, e^{i\mathbf{k}\cdot\mathbf{x}} \right)$$

$$= \widehat{\psi_{k_r}^*} \, e^{-i\mathbf{k}_r\cdot\mathbf{x}} \left(\sum_{\mathbf{k}} \frac{\partial}{\partial t} \widehat{\zeta_k} \, e^{i\mathbf{k}\cdot\mathbf{x}} + \sum_{\mathbf{k}} \widehat{A_k} \, e^{i\mathbf{k}\cdot\mathbf{x}} \right).$$
(C3)

Since Fourier modes are orthogonal, only the following remains:

$$\widehat{\psi_{k_r}^*} \, e^{-i\mathbf{k}_r\cdot\mathbf{x}} \left(\sum_{\mathbf{k}} \frac{\partial}{\partial t} \widehat{\zeta_k} \, e^{i\mathbf{k}\cdot\mathbf{x}} + \sum_{\mathbf{k}} \widehat{A_k} \, e^{i\mathbf{k}\cdot\mathbf{x}} \right) = \widehat{\psi_{k_r}^*} \frac{\partial}{\partial t} \widehat{\zeta_{k_r}} + \widehat{\psi_{k_r}^*} \widehat{A_{k_r}}.$$
(C4)

The first term on the right-hand side accounts for the time derivative of the kinetic energy at one wavenumber. We note that from equation Eq. (C4), we obtain a 2D spectrum because the wavenumbers are divided into a zonal part and a meridional part. Before further computation, an azimuthal average is performed on the 2D spectrum to obtain a 1D spectrum, and the 1D wavenumbers obtained thus correspond to the radial wavenumbers of the 2D spectrum: From $\mathbf{k}_r = (k_r, l_r)$, we obtain $r = k_r^2 + l_r^2$.

Now including the forcing and dissipation term initially appearing in the relative vorticity equation, we obtain

$$\frac{\partial \widehat{KE_r}}{\partial t} = -\widehat{\psi_r^*} \widehat{A_r} - \underbrace{f_0 \widehat{\psi_r^*} \frac{\partial \widehat{w_r}}{\partial z}}_{\widehat{w}^* \widehat{b}} + \widehat{\psi_r^*} F_{w_r} + \widehat{\psi_r^*} \widehat{D_r}.$$
(C5)

The interest behind this demonstration is to obtain an expression for the spectral fluxes, meaning at which wavenumber energy from a reservoir is leaked or inserted due to a certain term. For the specific case of potential-to-kinetic energy conversion term wb, it is of interest to further consider the spectral estimate of w which, in QG, can be expressed through the density equation as

$$w = \frac{1}{N^2} (\partial_t + \mathbf{u}_g \cdot \boldsymbol{\nabla}_h) (\underbrace{f_0 \partial_z \psi}_{=b}).$$
(C6)

The advective component of w can then be written in terms of buoyancy $b = f_0 \partial_z \psi$ and streamfunction ψ as

$$w^{(\text{adv})} = \frac{1}{N^2} J(\psi, b),$$
(C7)

with $J(A, B) = \partial_x A \partial_y B - \partial_x B \partial_y A$ as the Jacobian operator. Expressing the streamfunction and the buoyancy in Fourier modes, i.e., $\psi = \sum_{\mathbf{p}} \hat{\psi}(\mathbf{p}, t) e^{i\mathbf{p}\cdot\mathbf{x}}$ and $b = \sum_{\mathbf{q}} \hat{b}(\mathbf{q}, t) e^{i\mathbf{q}\cdot\mathbf{x}}$, we can then express the (conjugate of) Fourier transform of w as

$$\hat{w}^* = \frac{1}{N^2} J(\widehat{\psi, b})^* = \frac{1}{N^2} \left[\sum_{\mathbf{p}} p^x \hat{\psi}(\mathbf{p}, t) e^{i\mathbf{p}\cdot\mathbf{x}} \sum_{\mathbf{q}} q^y \hat{b}(\mathbf{q}, t) e^{i\mathbf{q}\cdot\mathbf{x}} - \sum_{\mathbf{p}} p^y \hat{\psi}(\mathbf{p}, t) e^{i\mathbf{p}\cdot\mathbf{x}} \sum_{\mathbf{q}} q^x \hat{b}(\mathbf{q}, t) e^{i\mathbf{q}\cdot\mathbf{x}} \right]^*$$

$$= \frac{1}{N^2} \int \left[\sum_{\mathbf{p},\mathbf{q}} (p^x q^y - p^y q^x) \hat{\psi}\hat{b} e^{-i(\mathbf{p}+\mathbf{q})\cdot\mathbf{x}} \right] e^{i\mathbf{k}\cdot\mathbf{x}} \, d\mathbf{x} = \frac{1}{N^2} \sum_{\mathbf{p},\mathbf{q}} A(\mathbf{p}, \mathbf{q}, \mathbf{k}) \hat{\psi}\hat{b}, \tag{C8}$$

with $A(\mathbf{p}, \mathbf{q}, \mathbf{k}) = (p^x q^y - p^y q^x)\delta(\mathbf{k} - \mathbf{p} - \mathbf{q})$ as an "interaction coefficient" similar to what can be derived for the advective term in QG [see Vallis (2006)]. Upon multiplication by $\hat{b}$ to obtain a spectral estimate of wb, we can then identify a cross-scale KE transfer. Azimuthally averaging the obtained two-dimensional power spectral provides spectral estimates of energy conversion repartition across different scales. However, the resulting spectra are hardly readable because of steep variations along small range of wavenumber, and it is common to instead perform a wavenumber integration assuming that the flux vanishes at the highest wavenumber (Arbic et al. 2013), such that

$$\Pi_{wb}(\mathbf{k}) = \int_{\mathbf{k}}^{\infty} \hat{w}^* \hat{b} \, d\mathbf{k}. \tag{C9}$$

Formally, this should be interpreted as the net contribution of energy fluxes from smallest resolved scales to the scale associated with wavenumber $\mathbf{k}$. Previously, a positive value of wb meant a conversion from potential energy to kinetic energy; now, it is represented by a negative slope.

APPENDIX D

Effects of Relative Wind Stress on Wind Work

We briefly review here the demonstration that relative wind stress formulation leads to a sign definite contribution in wind work. This demonstration is largely inspired by that of Zhai and Greatbatch (2007). We note, however, that no assumptions of scale, amplitude, nor direction of atmospheric winds and ocean surface currents are made here, as opposed to, e.g., Duhaut and Straub (2006).

Consider the wind works WW_1 and WW_2, defined as

$$WW^{(1,2)} = \boldsymbol{\tau}^{(1,2)} \cdot \rho_0 \mathbf{u}_o, \tag{D1}$$

with the wind stress $\boldsymbol{\tau}^{(1)}$ defined with an *absolute* formulation [Eq. (2)] and $\boldsymbol{\tau}^{(2)}$ defined with a *relative* formulation [Eq. (1)]. We want to evaluate the sign of the energy changes induced by the ocean current feedback. For this, consider the change in wind work (ignoring potential changes in drag coefficients C_d and atmospheric wind $\mathbf{u}_a$):

$$\frac{\Delta WW}{\rho_0 \rho_a C_d} = \frac{WW^{(2)} - WW^{(1)}}{\rho_0 \rho_a C_d}$$

$$= \underbrace{(|\mathbf{u}_a - \mathbf{u}_o| - |\mathbf{u}_a|)\mathbf{u}_a \cdot \mathbf{u}_o}_{A} - \underbrace{|\mathbf{u}_a - \mathbf{u}_o|\mathbf{u}_o \cdot \mathbf{u}_o}_{B}. \tag{D2}$$

One can easily show that $B > 0$ for all conditions (i.e., both $|\mathbf{u}_a - \mathbf{u}_o|$ and $\mathbf{u}_o \cdot \mathbf{u}_o$ are positive definite); thus, it represents a sink of energy ($-B < 0$). However, the sign definiteness of A is less obvious, and two scenarios should be considered depending on the sign of $\mathbf{u}_a \cdot \mathbf{u}_o$.

We first consider the case when $\mathbf{u}_a \cdot \mathbf{u}_o < 0$, which would imply that $(|\mathbf{u}_a - \mathbf{u}_o| > |\mathbf{u}_a|)$ for A to be sign definite and negative (i.e., a sink of energy). Squaring the later inequality leads to

$$|\mathbf{u}_a|^2 < |\mathbf{u}_a - \mathbf{u}_o|^2, \tag{D3a}$$

$$\mathbf{u}_a \cdot \mathbf{u}_a < (\mathbf{u}_a - \mathbf{u}_o) \cdot (\mathbf{u}_a - \mathbf{u}_o), \tag{D3b}$$

$$\mathbf{u}_a \cdot \mathbf{u}_o < \frac{1}{2}\mathbf{u}_o \cdot \mathbf{u}_o. \tag{D3c}$$

Inequality equation [Eq. (D3c)] is valid for $\mathbf{u}_a \cdot \mathbf{u}_o < 0$ (our current condition) since surface kinetic energy $(1/2)\mathbf{u}_o \cdot \mathbf{u}_o$ is defined positive.

However, if $\mathbf{u}_a \cdot \mathbf{u}_o > 0$, the condition of having sign definite (i.e., a sink of energy) for A requires

$$|\mathbf{u}_a| > |\mathbf{u}_a - \mathbf{u}_o|, \tag{D4}$$

leading to (once squared)

$$\mathbf{u}_a \cdot \mathbf{u}_o > \frac{1}{2}\mathbf{u}_o \cdot \mathbf{u}_o. \tag{D5}$$

Thus, in the case where $0 < \mathbf{u}_a \cdot \mathbf{u}_o < (1/2)\mathbf{u}_o \cdot \mathbf{u}_o$, the contribution of A is a source of kinetic energy for the ocean. This is satisfied only in specific conditions; i.e., when wind and currents are in the same direction (defined on a $[-\pi/2; \pi/2]$ orientation centered with $\mathbf{u}_a$ or $\mathbf{u}_0$), the *relative* wind work will induce a source of kinetic energy for the ocean surface current if the dot product of atmospheric winds with oceanic surface currents is weaker than the kinetic energy of the ocean surface currents. This can be associated with either weak wind conditions or wind conditions nearly orthogonal to the ocean surface currents. Nonetheless, although A is not always sign definite and can contribute positively to ocean kinetic energy, such positive contribution will remain weaker than that of B such that the overall wind work difference induced by ocean surface current will always act as a sink of energy for the ocean. This last statement has been verified numerically (not shown).

REFERENCES

Arbic, B. K., K. L. Polzin, R. B. Scott, J. G. Richman, and J. F. Shriver, 2013: On eddy viscosity, energy cascades, and the horizontal resolution of gridded satellite altimeter products. *J. Phys. Oceanogr.*, **43**, 283–300, https://doi.org/10.1175/JPO-D-11-0240.1.

Capet, X., J. C. McWilliams, M. J. Molemaker, and A. F. Shchepetkin, 2008: Mesoscale to submesoscale transition in the California Current System. Part I: Flow structure, eddy flux, and observational tests. *J. Phys. Oceanogr.*, **38**, 29–43, https://doi.org/10.1175/2007JPO3671.1.

Chen, R., G. R. Flierl, and C. Wunsch, 2014: A description of local and nonlocal eddy–mean flow interaction in a global eddy-permitting state estimate. *J. Phys. Oceanogr.*, **44**, 2336–2352, https://doi.org/10.1175/JPO-D-14-0009.1.

Dawe, J. T., and L. Thompson, 2006: Effect of ocean surface currents on wind stress, heat flux, and wind power input to the ocean. *Geophys. Res. Lett.*, **33**, L09604, https://doi.org/10.1029/2006GL025784.

Deremble, B., T. Uchida, W. K. Dewar, and R. Samelson, 2023: Eddy-mean flow interaction with a multiple scale quasi geostrophic model. *J. Adv. Model. Earth Syst.*, **15**, e2022MS003572, https://doi.org/10.1029/2022MS003572.

Dewar, W. K., and G. R. Flierl, 1987: Some effects of the wind on rings. *J. Phys. Oceanogr.*, **17**, 1653–1667, https://doi.org/10.1175/1520-0485(1987)017<1653:SEOTWO>2.0.CO;2.

Duhaut, T. H. A., and D. N. Straub, 2006: Wind stress dependence on ocean surface velocity: Implications for mechanical energy input to ocean circulation. *J. Phys. Oceanogr.*, **36**, 202–211, https://doi.org/10.1175/JPO2842.1.

Gaube, P., D. B. Chelton, R. M. Samelson, M. G. Schlax, and L. W. O'Neill, 2015: Satellite observations of mesoscale eddy-induced Ekman pumping. *J. Phys. Oceanogr.*, **45**, 104–132, https://doi.org/10.1175/JPO-D-14-0032.1.

Harrison, D. E., and A. R. Robinson, 1978: Energy analysis of open regions of turbulent flows—Mean eddy energetics of a numerical ocean circulation experiment. *Dyn. Atmos. Oceans*, **2**, 185–211, https://doi.org/10.1016/0377-0265(78)90009-X.

Hogg, A., J. Blundell, W. Dewar, and P. Killworth, 2014: Formulation and users' guide for Q-GCM. http://q-gcm.org/downloads.html.

Hogg, A. M. C., W. K. Dewar, P. D. Killworth, and J. R. Blundell, 2006: Decadal variability of the midlatitude climate system driven by the ocean circulation. *J. Climate*, **19**, 1149–1166, https://doi.org/10.1175/JCLI3651.1.

Jamet, Q., B. Deremble, N. Wienders, T. Uchida, and W. K. Dewar, 2021: On wind-driven energetics of subtropical gyres. *J. Adv. Model. Earth Syst.*, **13**, e2020MS002329, https://doi.org/10.1029/2020MS002329.

——, S. Leroux, W. K. Dewar, T. Penduff, J. Le Sommer, J.-M. Molines, and J. Gula, 2022: Non-local eddy-mean kinetic energy transfers in submesoscale-permitting ensemble simulations. *J. Adv. Model. Earth Syst.*, **14**, e2022MS003057, https://doi.org/10.1029/2022MS003057.

Jullien, S., S. Masson, V. Oerder, G. Samson, F. Colas, and L. Renault, 2020: Impact of ocean–atmosphere current feedback on ocean mesoscale activity: Regional variations and sensitivity to model resolution. *J. Climate*, **33**, 2585–2602, https://doi.org/10.1175/JCLI-D-19-0484.1.

Kang, D., and E. N. Curchitser, 2015: Energetics of eddy–mean flow interactions in the Gulf Stream region. *J. Phys. Oceanogr.*, **45**, 1103–1120, https://doi.org/10.1175/JPO-D-14-0200.1.

Lorenz, E. N., 1955: Available potential energy and the maintenance of the general circulation. *Tellus*, **7A**, 157–167, https://doi.org/10.3402/tellusa.v7i2.8796.

Ma, X., and Coauthors, 2016: Western boundary currents regulated by interaction between ocean eddies and the atmosphere. *Nature*, **535**, 533–537, https://doi.org/10.1038/nature18640.

Martin, P. E., B. K. Arbic, A. M. Hogg, A. E. Kiss, J. R. Munroe, and J. R. Blundell, 2020: Frequency-domain analysis of the energy budget in an idealized coupled ocean–atmosphere model. *J. Climate*, **33**, 707–726, https://doi.org/10.1175/JCLI-D-19-0118.1.

Matsuta, T., and Y. Masumoto, 2021: Modified view of energy budget diagram and its application to the Kuroshio extension region. *J. Phys. Oceanogr.*, **51**, 1163–1175, https://doi.org/10.1175/JPO-D-20-0124.1.

——, and ——, 2023: Energetics of the Antarctic circumpolar current. Part I: The Lorenz energy cycle and the vertical energy redistribution. *J. Phys. Oceanogr.*, **53**, 1467–1484, https://doi.org/10.1175/JPO-D-22-0133.1.

McCaffrey, K., B. Fox-Kemper, and G. Forget, 2015: Estimates of ocean macroturbulence: Structure function and spectral slope from Argo profiling floats. *J. Phys. Oceanogr.*, **45**, 1773–1793, https://doi.org/10.1175/JPO-D-14-0023.1.

Murakami, S., 2011: Atmospheric local energetics and energy interactions between mean and eddy fields. Part I: Theory. *J. Atmos. Sci.*, **68**, 760–768, https://doi.org/10.1175/2010JAS3664.1.

Oort, A. H., L. A. Anderson, and J. P. Peixoto, 1994: Estimates of the energy cycle of the oceans. *J. Geophys. Res.*, **99**, 7665–7688, https://doi.org/10.1029/93JC03556.

Pacanowski, R. C., 1987: Effect of equatorial currents on surface stress. *J. Phys. Oceanogr.*, **17**, 833–838, https://doi.org/10.1175/1520-0485(1987)017<0833:EOECOS>2.0.CO;2.

Renault, L., M. J. Molemaker, J. Gula, S. Masson, and J. C. McWilliams, 2016: Control and stabilization of the gulf stream by oceanic current interaction with the atmosphere. *J. Phys. Oceanogr.*, **46**, 3439–3453, https://doi.org/10.1175/JPO-D-16-0115.1.

——, P. Marchesiello, S. Masson, and J. C. Mcwilliams, 2019: Remarkable control of western boundary currents by *Eddy Killing*, a mechanical air-sea coupling process. *Geophys. Res. Lett.*, **46**, 2743–2751, https://doi.org/10.1029/2018GL081211.

Roullet, G., J. C. Mcwilliams, X. Capet, and M. J. Molemaker, 2012: Properties of steady geostrophic turbulence with isopycnal outcropping. *J. Phys. Oceanogr.*, **42**, 18–38, https://doi.org/10.1175/JPO-D-11-09.1.

Seo, H., and Coauthors, 2023: Ocean mesoscale and frontal-scale ocean–atmosphere interactions and influence on large-scale climate: A review. *J. Climate*, **36**, 1981–2013, https://doi.org/10.1175/JCLI-D-21-0982.1.

Song, H., J. Marshall, D. J. McGillicuddy Jr., and H. Seo, 2020: Impact of current-wind interaction on vertical processes in the Southern Ocean. *J. Geophys. Res. Oceans*, **125**, e2020JC016046, https://doi.org/10.1029/2020JC016046.

Uchida, T., B. Deremble, and S. Popinet, 2022: Deterministic model of the eddy dynamics for a midlatitude ocean model. *J. Phys. Oceanogr.*, **52**, 1133–1154, https://doi.org/10.1175/JPO-D-21-0217.1.

Vallis, G. K., 2006: *Atmospheric and Oceanic Fluid Dynamics: Fundamentals and Large-Scale Circulation.* Cambridge University Press, 745 pp.

Waterman, S., and S. R. Jayne, 2011: Eddy-mean flow interactions in the along-stream development of a western boundary current jet: An idealized model study. *J. Phys. Oceanogr.*, **41**, 682–707, https://doi.org/10.1175/2010JPO4477.1.

Zhai, X., and R. J. Greatbatch, 2007: Wind work in a model of the northwest Atlantic Ocean. *Geophys. Res. Lett.*, **34**, L04606, https://doi.org/10.1029/2006GL028907.

Zhu, Y., Y. Li, Y. Yang, and F. Wang, 2023: The role of eddy-wind interaction in the eddy kinetic energy budget of the Agulhas retroflection region. *Environ. Res. Lett.*, **18**, 104032, https://doi.org/10.1088/1748-9326/acfb9a.